SOFT ROBOTICS
Volume 4, Number 3, 2017

DOI: 10.1089/soro.2016.0056

SoRo
Soft Robotics

ORIGINAL ARTICLE

Smart Braid Feedback for the Closed-Loop Control of Soft Robotic Systems

Wyatt Felt, Khai Yi Chin, and C. David Remy

Abstract

This article experimentally investigates the potential of using flexible, inductance-based contraction sensors in the closed-loop motion control of soft robots. Accurate motion control remains a highly challenging task for soft robotic systems. Precise models of the actuation dynamics and environmental interactions are often unavailable. This renders open-loop control impossible, while closed-loop control suffers from a lack of suitable feedback. Conventional motion sensors, such as linear or rotary encoders, are difficult to adapt to robots that lack discrete mechanical joints. The rigid nature of these sensors runs contrary to the aspirational benefits of soft systems. As truly soft sensor solutions are still in their infancy, motion control of soft robots has so far relied on laboratory-based sensing systems such as motion capture, electromagnetic (EM) tracking, or Fiber Bragg Gratings. In this article, we used embedded flexible sensors known as Smart Braids to sense the contraction of McKibben muscles through changes in inductance. We evaluated closed-loop control on two systems: a revolute joint and a planar, one degree of freedom continuum manipulator. In the revolute joint, our proposed controller compensated for elasticity in the actuator connections. The Smart Braid feedback allowed motion control with a steady-state root-mean-square (RMS) error of [1.5]°. In the continuum manipulator, Smart Braid feedback enabled tracking of the desired tip angle with a steady-state RMS error of [1.25]°. This work demonstrates that Smart Braid sensors can provide accurate position feedback in closed-loop motion control suitable for field applications of soft robotic systems.

Keywords: Smart Braid, inductance sensing, McKibben muscle, pneumatic, closed-loop control

Introduction

The motion of many soft systems is often controlled in a purely open-loop manner[1–3] or through manual teleoperation.[4] In some systems, the primary objective may be to exert forces on the environment with little concern for the robot pose. In other systems, such as manipulators, measuring and controlling the robot pose are essential. Open-loop control can be very effective if the system is well known, no external disturbances are present, and positional accuracy is not imperative. The approach fails, however, if the system is subject to unknown forces or constraints from the environment, we cannot obtain a precise system model, or are unable to invert this model due to hysteresis or other nonlinear effects.[5] To perform motion control under such circumstances, closed-loop feedback becomes imperative. As the field of soft robotics matures, there is consequently an increasing interest in transforming soft *mechanisms* into soft *robots* that can measure and control their own motion.[6–11]

Despite recent advances, practical closed-loop motion control of soft robotic systems remains a challenge.[12–14] The pose of many soft systems is difficult to measure with sensors common to rigid robots such as rotary and linear encoders. Soft robotic systems rarely provide convenient coupling points for such sensors. For example, the control of a soft, assistive device (Fig. 1a) might require sensing of human joint motion where the joint cannot be accessed directly. For a continuum manipulator, the problem is even more challenging, as motion is distributed throughout the entire system and no discrete joint axis exists (Fig. 1b).

Current methods for sensing soft systems can be divided roughly into three categories: external localization, curvature sensing, and length sensing. External localization systems include, for example, camera-based 3D motion capture,

Robotics and Motion Laboratory (RAMlab), Department of Mechanical Engineering, University of Michigan, Ann Arbor, Michigan.

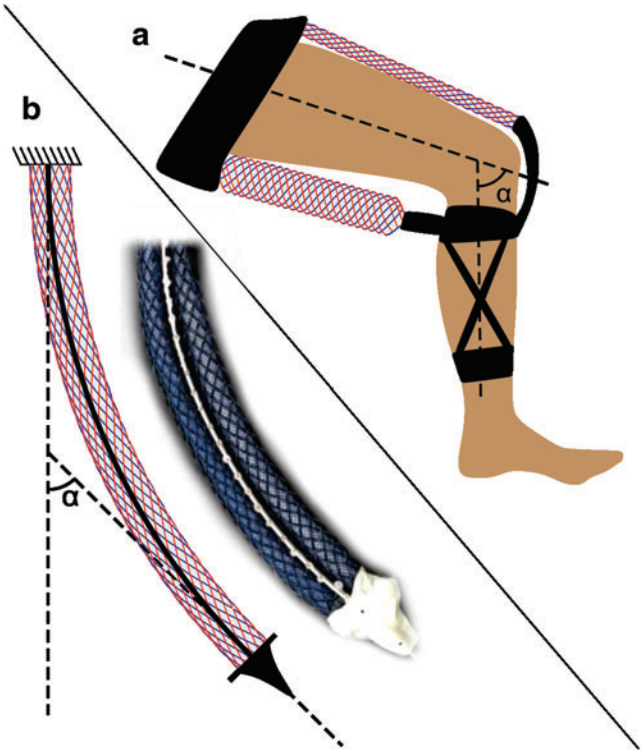

FIG. 1. Shown are two examples of soft robotic systems: **(a)** a soft orthosis that assists in creating torques about a human knee and **(b)** a one degree of freedom continuum manipulator. In each case, the systems are not readily sensed by traditional, rigid sensors. In this work, we propose the use of soft, flexible sensors to provide feedback control for systems like these. In particular, we used pneumatic McKibben muscles with inductance-based ''Smart Braid'' sensors on their exterior to measure actuator lengths. Closed-loop feedback was enabled and experimentally evaluated in the control of two bench-top systems analogous to those depicted in this study. Color images available online at www.liebertpub.com/soro

which has been used to provide feedback for continuum manipulators,[6,7] and an inflatable humanoid.[8] A similar technology is based on electromagnetic trackers.[9,10] Curvature sensing is appropriate when soft robot motion corresponds to the bending of inextensible portions such as flexible ''spines.'' For such systems, a variety of curvature sensors exist.[15] For example, optical systems can measure curvature by measuring the attenuation of transmitted light.[16,17] Other systems measure curvature through the Hall effect of a nearby magnet[18] or piezoelectric effects.[19]

Finally, a soft robot's pose can be estimated by measuring changes in the length of paths along the continuously deformable structure. For example, one can measure the deformation of a continuum manipulator by measuring the displacement of inextensible strings alongside the lengths of the sections.[20–23] A number of alternative sensors have been proposed to measure such changes in length. Fiber Bragg Gratings, for example, can detect strains in optical fibers. The strain changes the spacing of the gratings and the corresponding reflected wavelength. Groups of fibers can register curvature through changes in the fiber strains.[11,24] These sensors have been used as feedback for the control of continuum devices.[11,25–27] The strain measurable by these sensors is limited to the tensile strain that the optical fibers can undergo. A number of sensors are based on registering a change in electrical resistance under strain. The resistive element may be an elastomer[28,29] and microchannels of conductive liquid[30–32] or a conductive fabric.[33] Strain measurements can also come from the capacitance of specially formed ''dielectric elastomers.''[34–37] These elastomers can provide both actuation force and strain measurements through the changing separation of flexible electrodes.[38] In addition, we have shown in our prior work how inductance-based sensors can be used to measure the length of soft actuators.[39–41]

In this article, we used flexible sensors built into the structure of soft actuators to provide feedback for the motion control of two soft robotic systems. The first system was a revolute joint (Fig. 2). This allowed us to rigorously compare the efficacy of feedback from our sensors to that from a rotary encoder. This system is also an example of applications with a well-defined joint axis, yet in which the joint angle is difficult to measure, for example, in an assistive robotic device for an elbow or knee joint (Fig. 1a). The second system we tested was a planar, one degree of freedom continuum manipulator (Fig. 1b). This system highlights the ability of flexible sensors to enable the motion feedback control of systems without rigid joints.

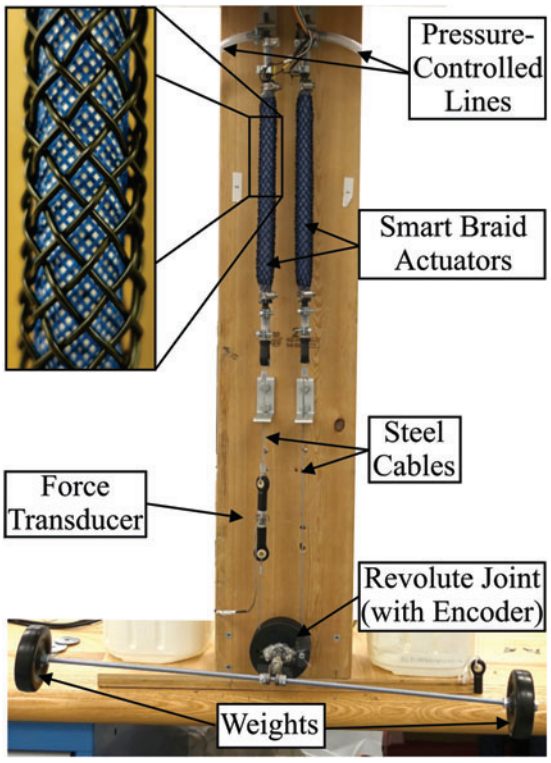

FIG. 2. A one degree of freedom revolute joint allowed us to compare two types of feedback control: one based on measurements from a rotary encoder and another based on measurements from Smart Braid sensors. The Smart Braid sensors used in this work were placed on *top* of an inner, nonconductive reinforcing braid (enlarged detail, *black wires* are conductive, *blue fibers* are polyester). A force transducer in series with the connection to the left actuator measured the tension in the connection cable. Color images available online at www.liebertpub.com/soro

The soft robotic systems that we evaluated were driven by McKibben muscles. McKibben muscles consist of an elastomeric bladder surrounded by a braided sheath.[42,43] The braided sheaths used in this work shaped the expansion of the elastic bladder into a forceful contraction. McKibben muscles' soft nature and high force density have led to their widespread application in human-assistive devices.[44–48] They have also been successfully employed in a range of continuum manipulators.[20,49,50]

In this work, the length of each McKibben muscle was measured through the inductance of a braided circuit that surrounded the actuator. As the actuator contracts, the inductance of the circuit increases. This increase in inductance is approximately linear with respect to the actuator length.[40] We refer to the circuit as a ''Smart Braid'' sensor. It is formed from off-the-shelf, insulated, conductive wires in a McKibben muscle pattern.[39] Smart Braid sensors do not require external cameras or antennas, and they are not limited to sensing the curvature of inextensible sections. They allow the length of the actuator to be measured without the additional force required to strain a self-sensing elastomer or the potential fragility introduced by optical fibers or strings.

The Smart Braid sensors used in this work were fabricated according to the process outlined in our previous work.[39] To improve the fatigue life of the sensors, the wires of the Smart Braid were isolated from the stress of actuation. This was accomplished by using an inner, polyester braid that reinforced the bladder against the internal pressure. The sensor braid was added over the top of this plastic braid. Both braids had similar fiber angles to create a similar contraction behavior.

This work presents the first demonstration of Smart Braid inductance sensors in the feedback control of robotic devices. Revolute Joint section includes the model, methods, and results of the revolute joint system. In this study, we propose a compensation method for compliance between length-sensing actuators (Smart Braid or otherwise) and the motion output. Continuum Manipulator section consists of a similar series of experiments on the continuum manipulator. Continuum Manipulator section also includes a model for Smart Braid sensors on continuum segments. Discussion and Conclusions section contains general discussion and conclusions.

Revolute Joint

The first example that we studied was a one degree of freedom revolute joint driven by antagonized McKibben muscles (Fig. 2). Smart Braid measurements of actuator length were used as feedback to control the joint angle. The controller actively compensated for the compliance in the actuator connections. The performance of this Smart Braid feedback controller was then compared to the performance of a similar controller that used feedback from a rotary encoder. This allowed us to perform a rigorous evaluation and comparison of the proposed Smart Braid feedback.

In the test fixture of the revolute joint, two Smart Braid McKibben muscles (Fig. 2) rotated a load by steel cables and a pulley with radius $r = 25.4$ mm (Fig. 3). The torque τ exerted on the load by the actuators was proportional to the difference between the two antagonized actuator forces, F_1 and F_2 (corresponding to actuators 1 and 2). The rotational inertia I of the load was $\sim 2 \times 10^{-3}$ kgm^2. Joint friction was modeled as viscous damping with a damping coefficient b of $\sim 1.2 \times 10^{-3}$ Nms. The inertia of the load primarily originated from two masses placed at the ends of a long rod. With the masses on separate ends of the rod (Fig. 4a), the center of mass of the load coincided with the axis of rotation with no resulting net torque from gravity. Shifting both masses to the same side (Fig. 4b, c) created a positive or negative load torque with a maximum magnitude of $\tau_{load} = 0.65$ Nm. In these configurations, the inertia of the system was approximately preserved.

Estimation of revolute joint angle with Smart Braids

The actuator neutral lengths $l_{neutral}$ were defined as the lengths of the actuators when the joint angle was 0° and the connections to the joint were without slack, but unstretched. The actuator contractions x were the deviations of the actuator lengths l away from $l_{neutral}$

$$\begin{aligned} x_1 &= l_{1,neutral} - l_1 \\ x_2 &= l_2 - l_{2,neutral}. \end{aligned} \tag{1}$$

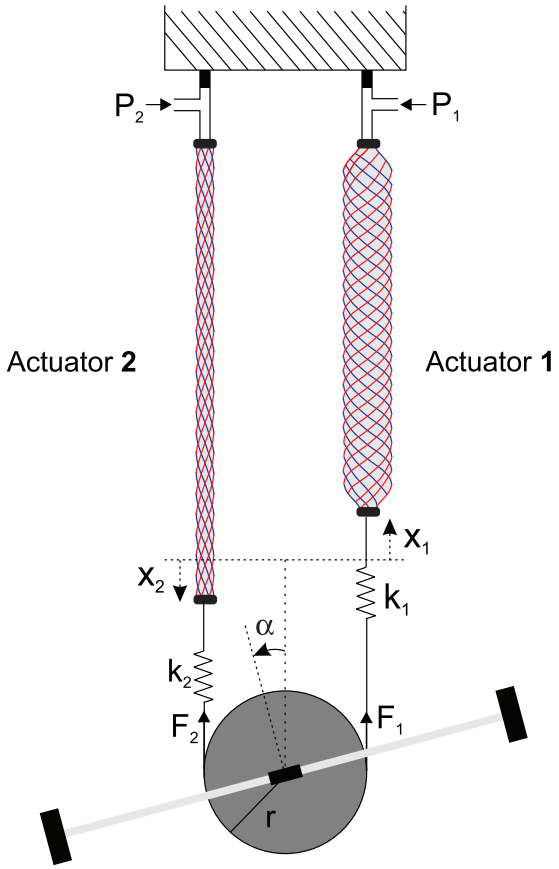

FIG. 3. When pressurized (with pressure values P_1 and P_2), the actuators in the revolute joint test fixture exerted forces F_1 and F_2. The difference in the two forces created a net torque on the rotating load that induced contractions in the actuators x_1 and x_2 and a rotation of the load (expressed by the angle α). The actuator connections were compliant and thus modeled as springs with linear stiffness k_1 and k_2. Color images available online at www.liebertpub.com/soro

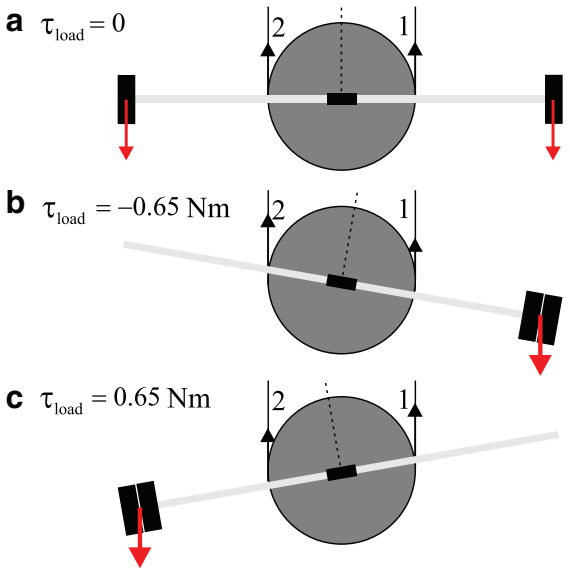

FIG. 4. The revolute joint consisted of a pulley connected to two masses at the ends of a thin rod. The controller was tested in each of three conditions: **(a)** with no load torque from gravity, **(b)** with a negative load torque, and **(c)** with a positive load torque. Color images available online at www.liebertpub.com/soro

For each actuator, a linear function of the inductance L was used to estimate the actuator contraction $x(L)$[40]

$$x_1(L_1) = a_{r1}L_1 + b_{r1}$$
$$x_2(L_2) = a_{r2}L_2 + b_{r2}. \quad (2)$$

If the connections between the actuator and joint were perfectly stiff, the length of the actuators could be used to directly determine the joint angle. Our prior work, however, suggests that measurements of joint motion can be skewed by compliance in mechanical couplings between the joint and actuator.[39,51] We thus compensated for this compliance by modeling the force output of the actuator and the compliance of the connection points. This compliance compensation used measurements of the actuator pressure to estimate the actuator force output. With the assumption that the connections were under tension, the displacement of the actuators was written in terms of the joint angle α and the output force F. This relationship took into account the stretching of the actuator connections (with stiffness k)

$$x_1 = r\alpha + \frac{F_1}{k_1}$$
$$x_2 = r\alpha - \frac{F_2}{k_2}. \quad (3)$$

The estimates of α that result from inverting these relationships will be most accurate when the forces F are small and the stiffnesses k of the connections are high.

Calibration of the revolute joint

To characterize the force, pressure, and contraction relationship of the actuators, an empirical function was used. It was based on the contraction ratio ϵ_i,[52] which is the normalized difference between the fully extended actuator length l_e and the current actuator length l_i

$$\epsilon_i = \frac{l_e - l_i}{l_e}. \quad (4)$$

The estimated actuator force output $\hat{F}_i$ was modeled as a polynomial that is linear with respect to actuator pressure P_i and quadratic with respect to the contraction ratio ϵ_i:

$$\hat{F}_i = p_{00} + p_{10}P_i + p_{01}\epsilon_i + p_{11}P_i\epsilon_i + p_{02}\epsilon_i^2. \quad (5)$$

To collect the necessary data for the calibration, the actuators were tested under a range of cable tensions and actuator pressure values. The tensions ranged between 5 and 30 N (with 5 N increments). At each tension level, the pressure of actuator 1 was set to each of a series of pressure values between 0.1 and .31 MPa for 30 s (in .035 MPa increments). During each 30 s period, the pressure in actuator 2 was adjusted automatically to create the desired tension. This adjustment process was driven by measurements of cable tension from the force transducer in line with actuator 2 (Fig. 2). In this way, data were collected at each combination of tension levels and actuator 1 pressures. After each combination of pressure and tension was tested on actuator 1, the process was repeated with actuator 2 at the fixed pressure values. In this case, the pressure in actuator 1 was adjusted to maintain the desired cable tension. The steady-state data from the last 15 s of each pressure–tension combination were used in the calibration.

The data from these experiments were used to identify the coefficients of Eq. (2) and the estimated connection stiffness $\hat{k}$ in Eq. (3) (Table 1). The data were also used to identify the coefficients of Eq. (5) (Table 2). Note that connections to actuator 2 were less stiff than those to actuator 1. This was caused by the additional, compliant cable ends used to include the force transducer in the cable (Fig. 2). The low values of the coefficient of determination R^2 in Table 2 result, in part, from hysteresis effects, which are not modeled,[52] and the noisy measurements from the force transducer.

Compliance compensation and feedback control of the revolute joint

The goal of the feedback controller was to regulate the joint angle α to a desired angle α_{des}. Based on this desired angle, the relationships in Eq. (3) defined the desired length x_{des} of each actuator as a function of estimated actuator force outputs $\hat{F}_i$ and estimated connection stiffnesses $\hat{k}_i$:

$$x_{1,des} = r\alpha_{des} + \frac{\hat{F}_1}{\hat{k}_1}$$
$$x_{2,des} = r\alpha_{des} + \frac{\hat{F}_2}{\hat{k}_2}. \quad (6)$$

The force estimates $\hat{F}_i$ in the compensation terms were found by evaluating Eq. (5) with measurements of current

TABLE 1. IDENTIFIED COEFFICIENTS FOR EQ. (2) AND (3)

	a_r (mm/μH)	b_r (mm)	$1/\hat{k}$ (mm/N)	R^2
Actuator 1	13.47	−89.417	0.0547	0.99942
Actuator 2	−13.881	86.979	0.110	0.99910

TABLE 2. IDENTIFIED COEFFICIENTS FOR EQ. (5)

	p_{00} (N)	p_{10} (N/MPa)	p_{01} (N)	p_{11} (N/MPa)	p_{02} (N)	R^2
Actuator 1	−24.312	518.76	−33.769	−1429.5	−285.66	0.66
Actuator 2	−37.934	788.98	−200.03	−2503.7	494.79	0.87

pressure and actuator length. Length measurements were obtained from inductance values using Eq. (2).

The difference between the desired and measured contraction of each individual actuator constituted the control error e_i:

$$e_i = \frac{x_{i,des} - x_i(L_i)}{r}. \tag{7}$$

This error was normalized by the pulley radius r to yield values in units of joint angle. The complete compensation process is illustrated in Figure 5.

A separate PID controller for each actuator regulated the position errors e_i by commanding desired actuator forces $F_{i,des}$ (Fig. 6). To maintain tension in both actuators, an equal ''preload'' force F_{pre} was added to each desired force value. Different levels of preload were evaluated experimentally. Because the actuators are unable to create negative forces, both $F_{i,des}$ were saturated to be positive:

$$\begin{aligned} F_{1,des} &= \max\left(k_p e_1 + k_d \dot{e}_1 + k_i \int e_1 + F_{pre}, 0\right) \\ F_{2,des} &= \max\left(-k_p e_2 - k_d \dot{e}_2 - k_i \int e_2 + F_{pre}, 0\right). \end{aligned} \tag{8}$$

By inverting Eq. (5), the desired forces $F_{i,des}$ were converted into desired pressure values for each actuator $P_{i,des}$ and sent to pressure-control valves.

The performance of the Smart Braid feedback was compared to feedback from a rotary encoder on the joint. When using the encoder for feedback, the actuator-specific error value was simply the difference between the desired angle α_{des} and the measured angle $\alpha_{measured}$

$$e_1 = e_2 = \alpha_{des} - \alpha_{measured}. \tag{9}$$

This error was used in both PID controllers of Eq. (8). No compliance compensation had to be performed.

Experimental implementation, revolute joint

A Texas Instruments ''inductance-to-digital converter'' (TI LDC1612/4)[53] provided rapid measurements of the sensor inductance. This chip operates by exciting the natural frequency of a resonant tank circuit formed by an inductor and a capacitor in parallel. The Smart Braid sensors were connected in parallel with 390 pF capacitors. The series resistance of the Smart Braid sensors was ~0.3 ohms. The inductance values from the sensors had a target sampling rate of 1 kHz. An analysis of the inductance measurements from the Smart Braids in relaxed conditions showed a root-mean-square (RMS) noise level of 0.24 nH.

In the revolute joint test fixture, a digital incremental encoder (Koyo Electronics Industries; TRDA-2E2500VD) provided joint angle measurements with a quadrature resolution of 0.036°. The pulley radius r where the cables were connected to the revolute joint was 25.4 mm. A force transducer (Omega LC201-100) was attached serially to the steel cable of actuator 2. This was used to characterize the force–pressure relationship of the actuators, characterize the stiffness of the actuator connections, and measure preload tracking performance. The systems were controlled with custom scripts in LabVIEW. The measurements from the test apparatus were collected and processed with a data acquisition unit (NI PXIe-6341), which used a PXI express chassis (NI PXIe-1073) to communicate with LabVIEW. Inductance measurements were collected using an I2C bus (NI USB-8451). The mass flow rate into the actuator lines was controlled with proportional pneumatic valves (Enfield LS-V05 s). The pressure in each actuator line was measured with pressure transducers (WIKA A-10) with a [0.41]MPa range and controlled with a custom controller with compensation for the nonlinear aperture flow across the valves.[54] A 250 Hz LabVIEW loop acquired data from the pressure sensors and sent commands to the valves. The system pressure was limited to 0.31 MPa. Estimates of $\dot{e}$ were filtered with a five-point moving average. In the control loop, the measurements of

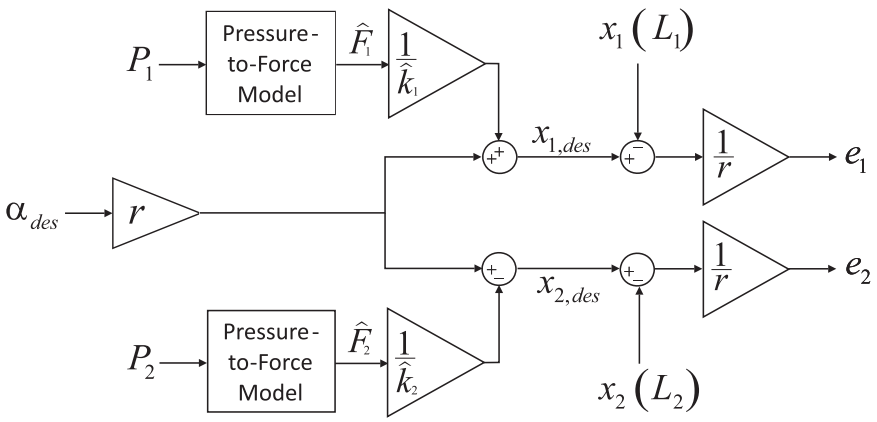

FIG. 5. The desired actuator contractions $x_{i,des}$ included a compensation term to account for stretching in the actuator connections. This compensation term was based on estimates of the force output $\hat{F}_i$ and the stiffness of the connections $\hat{k}_i$ of each actuator. The control error between the desired and measured contraction was scaled by the radius r of the pulley to yield a joint angle error e in units of radians.

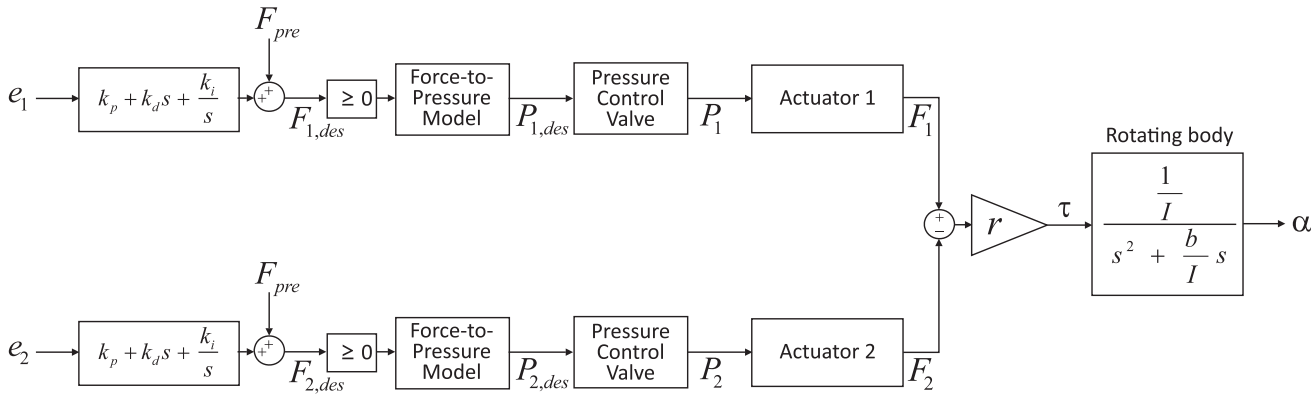

FIG. 6. For the revolute joint, two separate PID controllers commanded a desired force $F_{i,des}$ for each actuator in reaction to estimated joint angle error terms e_i. When the Smart Braids were used for feedback, e_i were determined individually from the measured inductance and pressure. When the encoder was used for feedback, e_i were equal. To generate the desired forces, the controller computed desired pressure values from a model of the actuator force-pressure-length relationship and sent these values to two pressure control valves.

inductance were filtered with a third-order low-pass Butterworth filter with a cutoff frequency of 10 Hz. To prevent excessive integrator windup, the product of the error integral and the integral gain was not permitted to exceed a magnitude of 50 N.

The two types of feedback were tested in random sequence at each of seven preload levels F_{pre}: 5 N, 7.5 N, 10 N, 12.5 N, 15 N, 17.5 N, and 20 N. Gains for each feedback type were selected by the ''some-overshoot'' Ziegler-Nichols method.[55] We first conducted a set of tuning trials in which gains were identified individually at each preload level. From the identified gains, the most conservative ones were subsequently used in the controller evaluation, where they were kept identical for all commanded preload levels (Table 3). This was done to ensure control stability in the event that the preload level did not match the commanded level.

Each controller configuration was tested on a fixed sequence of step changes for the desired joint angle α_{des}. The sequence was a random series of 21 angles between −30° and 30°, which were held for 10 s each. The data from the first 5 s of each step were considered ''transient'' and the data from the last 5 s were considered ''steady state.'' The performance was quantified by the RMS of the absolute error between the reference angle (α_{des}) and the angle measured by the encoder. During these tests, no load torque was applied (Fig. 4a). Each feedback type was tested at a given preload level thrice. Statistical significance between the feedback types was determined by paired t-tests across each of the commanded angles in the combined three tests. The values of the measured preload were averaged over the last 5 s of each step in the sequence.

Table 3. Gains for Revolute Joint Feedback Controller

Feedback type	k_p (N/rad)	k_d (N/(rad/s))	k_i (N/(rad s))
Encoder	19.80	3.4	74.05
Smart Braids	18.15	4.16	52.27

To evaluate the effectiveness of the compliance compensation in Eq. (6), the controller tests were repeated with the two load configurations that generated a nonzero net-torque (Fig. 3b, c). The unmodeled load torque renders open-loop control infeasible and stretches the actuator connections asymmetrically.

Results, revolute joint

Feedback control based entirely on soft, Smart Braid sensing is feasible. The Smart Braid feedback controller was able to track step changes in the commanded angle (Fig. 7). With no load torque, Smart Braid feedback led to an average RMS in the joint angle error of 1.73° (standard deviation [SD] 0.69°) during the last 5 s of each commanded angle (considered steady state, Fig. 8). The average RMS of the tracking error in the first 5 s of the commanded angles was 7.85° (SD 5.21°). Even with load torques of 0.65 Nm, the average steady-state error remained less than 2° (SD < 1°, Fig. 9).

The positional accuracy of the inductance feedback controller was comparable to the performance of a controller with feedback from the rotary encoder. During the first 5 s after a step change in the reference angle, the average RMS of the tracking error with encoder feedback was 6.60° (16% lower than with Smart Braid feedback, SD 4.56°, Fig. 7). Encoder feedback resulted in steady-state (during the last 5 s) errors with average RMS values between 0.8° and 1.3° depending on the load torque (SD < 0.8°, Fig. 9). This was smaller than the 1.5°–1.8° average RMS errors exhibited with Smart Braid feedback.

Figure 10 shows the measured preloads averaged over the last 5 s of each reference angle in the controlled trials (no load torque). With Smart Braid feedback, preloads of nearly 70 N were observed in the 12 N and 20 N conditions. The large preloads resulted from integral windup in the physically antagonized, yet independent, PID controllers.

Continuum Manipulator

As a second example, we investigated the use of Smart Braid feedback in a simple, planar, one degree of freedom manipulator driven by Smart Braid McKibben muscles

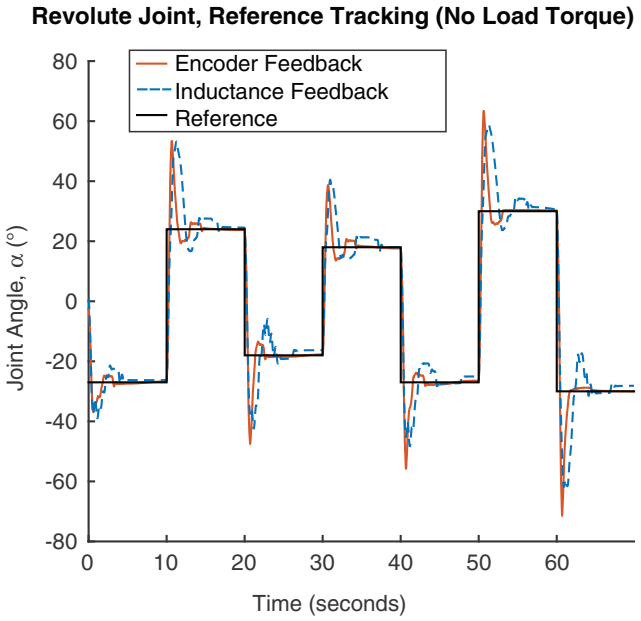

FIG. 7. Comparison of the effect of feedback type on the reference tracking of the revolute joint controller. On average, the encoder feedback (*red lines*) resulted in better joint angle tracking than the Smart Braid feedback (*blue lines*). During the first 5 s after the commanded step change, the average RMS of the error was 16% smaller in the encoder feedback case. In the last 5 s, the RMS of the encoder feedback error was, on average, 51% smaller than the Smart Braid error. In the case shown in this study, the desired preload was 10 N and no load torque was applied. Reported values were measured with the rotary encoder. RMS, root mean square. Color images available online at www.liebertpub.com/soro

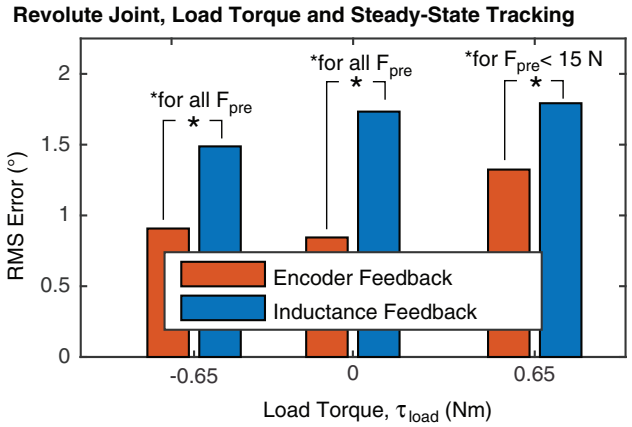

FIG. 9. Comparison of the steady-state error of the two feedback types used on the revolute joint under different load torque conditions. The height of the bars represents the averages of the RMS error across all the commanded preload levels during the last 5 s of each of each commanded angle. The average error with encoder feedback was always less than with inductance feedback. This difference was statistically significant ($p < .05$) in all cases except when $\tau_{load} = 0.65$ Nm and the desired preload was 15 N or higher. Color images available online at www.liebertpub.com/soro

(Fig. 11). The manipulator consisted of two contracting McKibben muscles connected along their length to a bendable ''spine.'' Differences in actuator pressure values caused different levels of contraction in the actuators, creating bending motions in the structure. By measuring the lengths of the actuators by Smart Braid inductance measurements, the degree of bending was estimated. This estimate was used as feedback to control the tip angle of the manipulator. This Smart Braid feedback control was compared to open-loop control based solely on actuator pressure.

Estimation of continuum manipulator tip angle with Smart Braids

The continuum manipulator was modeled as having a constant curvature enclosing an angle α. The length of the

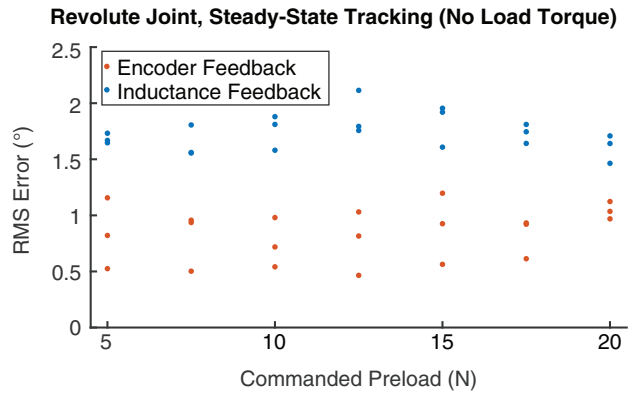

FIG. 8. Comparison of the steady-state error of the two feedback types used on the revolute joint under different preload conditions. Shown are the average RMS values across the three trials with no load torque. The vertical axis corresponds to the RMS of the reference error during the last 5 s of a commanded angle. The feedback from the encoder resulted in smaller errors in the steady-state tracking. Color images available online at www.liebertpub.com/soro

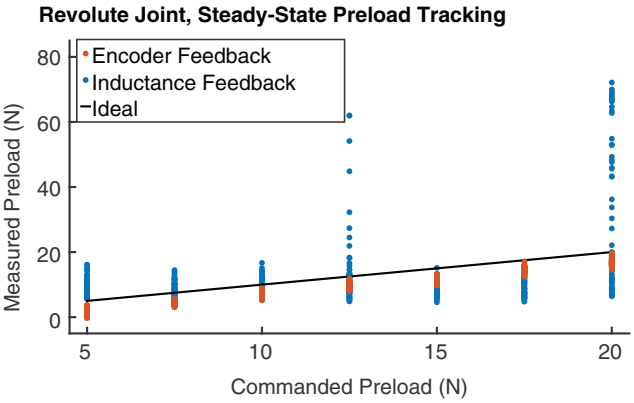

FIG. 10. Shown are the preloads on the revolute joint averaged over during the last 5 s of each commanded angle in the controlled trials. The two types of feedback resulted in different preloads. The effectual single integrator of the encoder feedback resulted in better preload tracking than the two integrators of the inductance feedback. For the conditions shown in this study, no load torque was applied. Color images available online at www.liebertpub.com/soro

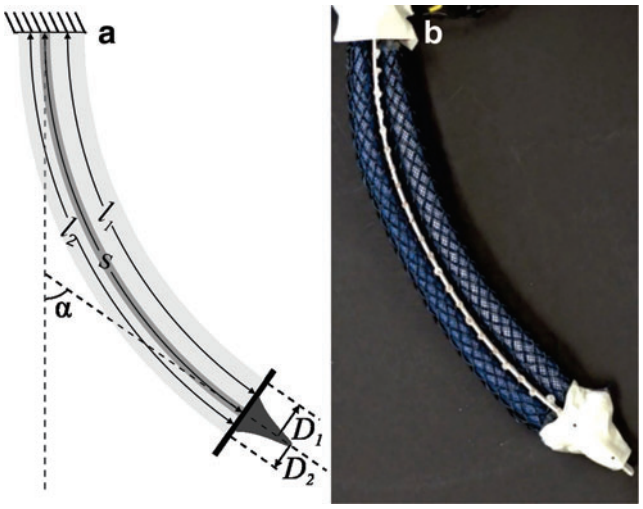

FIG. 11. The continuum manipulator. Two Smart Braid actuators were attached to a thin, flat flexible beam. Contracting the actuators caused the beam to bend. **(a)** The bend angle α was related to the lengths of the two actuators l_1 and l_2 and the fixed length s of the flexible spine. **(b)** The prototype device bending. Color images available online at www.liebertpub.com/soro

center of the manipulator was constant, constrained by a thin beam of length s. The braids of the two actuators on the sides were tied to the thin beam. The length of the actuators along their center lines l_i was related to the bending angle α by

$$\alpha = 2\frac{s - l_1}{D_1} = 2\frac{l_2 - s}{D_2} \tag{10}$$

where D_i is the diameter of the actuator cross-section. We assumed that the actuator radius was approximately the distance to the actuator centerline from the centerline of the thin beam.

McKibben muscles increase in diameter D as they contract. By approximating the shape of the McKibben muscle as a cylinder, the diameter D and centerline length l of the actuator were written in terms of the braid angle θ, the length b of fibers that make up the helices in the braid, and the number n of turns around the axis that each helix makes[39,43]

$$\begin{aligned} D &= \tfrac{b\sin\theta}{\pi n} \\ l &= b\cos\theta. \end{aligned} \tag{11}$$

These expressions were substituted for actuator 1 in Eq. (10) to relate the angle of the manipulator α to the braid angle θ_1:

$$\alpha = 2\pi n_1\left(\frac{s}{b_1\sin\theta_1} - \frac{1}{\tan\theta_1}\right). \tag{12}$$

The inductance of the Smart Braid sensors was approximated by considering the circuit formed by the wires to be a long solenoid.[39] The solenoid has a fixed number of turns N and a core with magnetic permeability μ. The inductance L of such a circuit will grow as the sensor contracts in length l and grows in cross-sectional area A

$$L = \mu\frac{N^2 A}{l}. \tag{13}$$

The number of turns in the solenoid circuit ($N = nn_h$) is the product of the number of turns n made by each helix and the number of helices n_h.

This approximation is appropriate even when the actuator is bent along its length. In this case, the circuit shape can be considered a segment of a toroidal inductor. The equation for the inductance of a toroid is identical to that of a straight long solenoid with a length equal to the circumference of the toroid centerline.

Equation (11) was used to express the inductance predicted by Eq. (13) in terms of the braid angle θ

$$L = \frac{\mu n_h^2 b}{4\pi}\sin\theta\tan\theta. \tag{14}$$

Inverting Eq. (12) results in the following expression for the braid angle on actuator 1 θ_1 in terms of the bend angle α

$$\begin{aligned} \theta_1 &= 2\tan^{-1}(\gamma(\alpha)) \\ \gamma(\alpha) &= \frac{\sqrt{\alpha^2 - \left(\frac{2\pi n_1 s}{b_1}\right)^2 + (2\pi n_1)^2} + \alpha}{(2\pi n_1)\left(\frac{s}{b_1} + 1\right)}. \end{aligned} \tag{15}$$

Note that the following expressions are true:

$$\begin{aligned} \sin(2\tan^{-1}(\gamma)) &= \tfrac{2\gamma}{\gamma^2+1} \\ \tan(2\tan^{-1}(\gamma)) &= \tfrac{-2\gamma}{\gamma^2-1}. \end{aligned} \tag{16}$$

Substituting Eq. (15) into Eq. (14) with the identities in Eq. (16) results in the following:

$$L_1(\alpha) = \left(\frac{\mu n_h^2 b_1}{4\pi}\right)\left(\frac{-4\gamma^2(\alpha)}{\gamma^4(\alpha) - 1}\right). \tag{17}$$

Equation (17) is defined for the inductance of the sensor on actuator 1. The inductance L_2 of the sensor on actuator 2 is given by evaluating Eq. (17) with $-\alpha$.

In the range we are interested in, Eq. (17) can be approximated as a quadratic function. We numerically evaluated Eq. (17) from $-90° \le \alpha \le 90°$ ($b_1 = 31$ cm, $n_h = 16$, $n_1 = 3.3$, $s = 26$ cm, $\mu = 4\pi\times10^{-7}$ H/m). A quadratic regression to the inductance response over this range had an R^2 value of 0.99999. Thus the inductance response of actuators 1 and 2 can be approximated as identical quadratic functions where $L_1(\alpha) = L_2(-\alpha)$

$$\begin{aligned} L_1(\alpha) &= f(\alpha) \approx \lambda_0 + \lambda_1\alpha + \lambda_2\alpha^2 \\ L_2(\alpha) &= f(-\alpha) \approx \lambda_0 - \lambda_1\alpha + \lambda_2\alpha^2. \end{aligned} \tag{18}$$

In the difference of L_1 and L_2, the quadratic terms are canceled and the linear terms are doubled

$$L_1 - L_2 = 2\lambda_1\alpha. \tag{19}$$

α can then be expressed as a linear function of L_1 and L_2

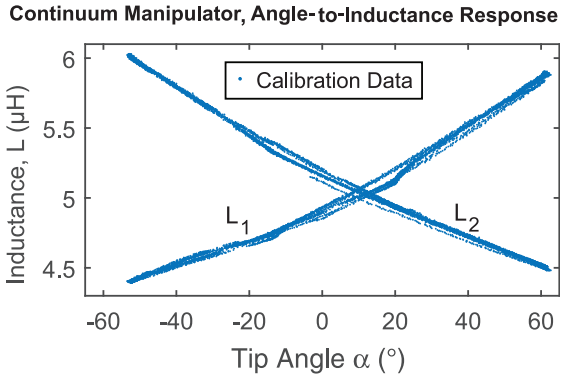

FIG. 12. Shown are the inductance values of the two actuators against the corresponding tip angle of the continuum manipulator. Inductance measurements are roughly quadratic with respect to the tip angle α. Color images available online at www.liebertpub.com/soro

$$\alpha(L_1, L_2) = \frac{1}{2\lambda_1} L_1 - \frac{1}{2\lambda_1} L_2. \tag{20}$$

In practice, the inductance response of the two Smart Braid actuators will not be identical (Fig. 12). Due to the manual fabrication process, the sensors and their connection to the flexible spine will be different. They may differ in the arc length s they enclose, the effective length b, or the number n of turns in their helices. These anticipated differences lead us to assume that the inductance response of two actuators will be best approximated by different quadratic functions:

$$\begin{aligned} L_1 &= \lambda_{01} + \lambda_{11}\alpha + \lambda_{21}\alpha^2 \\ L_2 &= \lambda_{02} - \lambda_{12}\alpha + \lambda_{22}\alpha^2. \end{aligned} \tag{21}$$

Still, the quadratic terms can be canceled

$$L_1 - \frac{\lambda_{21}}{\lambda_{22}} L_2 = \left(\lambda_{01} - \frac{\lambda_{21}}{\lambda_{22}}\lambda_{02}\right) + \left(\lambda_{11} + \frac{\lambda_{21}}{\lambda_{22}}\lambda_{12}\right)\alpha. \tag{22}$$

This leaves a form of α, which is a linear equation in two variables

$$\alpha_{est} = a_{c1} L_1 + a_{c2} L_2 + b_c. \tag{23}$$

Calibration, continuum manipulator

The control variable for the continuum manipulator was the pressure difference ΔP between the two actuators. From this difference, the desired pressure in each actuator was computed such that there always remained a minimal baseline pressure of P_{base}:

TABLE 4. IDENTIFIED COEFFICIENTS FOR EQ. (25)

a_{cp} (deg/MPa)	b_{cp} (deg)	R^2
597	3.45	0.826

TABLE 5. IDENTIFIED COEFFICIENTS FOR EQ. (23)

a_{c1} (deg/μH)	a_{c2} (deg/μH)	b_c (deg)	R^2
31.93	–45.11	77.08	0.999

$$\begin{aligned} P_{1,des} &= \begin{cases} P_{base} + \Delta P, & \Delta P > 0 \\ P_{base}, & \Delta P \le 0 \end{cases} \\ P_{2,des} &= \begin{cases} P_{base}, & \Delta P \ge 0 \\ P_{base} - \Delta P, & \Delta P < 0. \end{cases} \end{aligned} \tag{24}$$

The value of baseline pressure $P_{base} = 0.05$ MPa was selected to roughly correspond to the onset of actuator motion under no-load conditions.

To calibrate the continuum manipulator, ΔP was increased and decreased linearly between ~ -0.1 MPa and 0.1 MPa five times over the course of 10 min. Because of the slowly changing pressure values, the dynamics of the actuator motion were neglected. The calibration pressures were assumed to correspond to steady-state measured angles. These data were processed to identify a relationship between ΔP and α. The data were regressed to a linear approximation of the form

$$\alpha = a_{cp}\Delta P + b_{cp}. \tag{25}$$

The identified coefficients of Eq. (25) are listed in Table 4. The nonzero value of b_{cp} is indicative of the asymmetry in the system. The angle to pressure relationship exhibited hysteresis and nonlinearity (Fig. 16). Different pressure values often resulted in the same tip angle. This is apparent in the large degree of variation in the angle that is not captured by the linear model ($R^2 = 0.826$).

The calibration data were also used to identify a relationship between the continuum angle and the measured inductance of the Smart Braid actuators (Fig. 12). A two-variable linear regression was used to identify the coefficients of Eq. (23). They are listed in Table 5. The RMS of the residual error was 1.17° (Fig. 13).

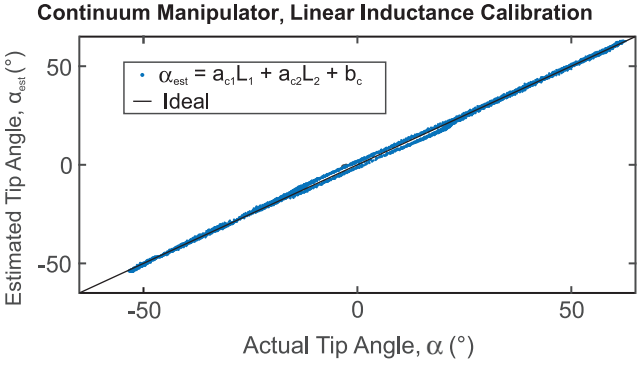

FIG. 13. Shown are the estimated values of the tip angle ($\alpha_{est} = a_{c1}L_1 + a_{c2}L_2 + b_c = 31.93L_1 - 45.11L_2 + 77.08$) from the inductance values used in the calibration. These values are compared against the tip angle recorded by the camera. The quadratic terms in the sensor response of the individual Smart Braids (Fig. 12) are fully compensated by a linear combination of both inductance measurements. Color images available online at www.liebertpub.com/soro

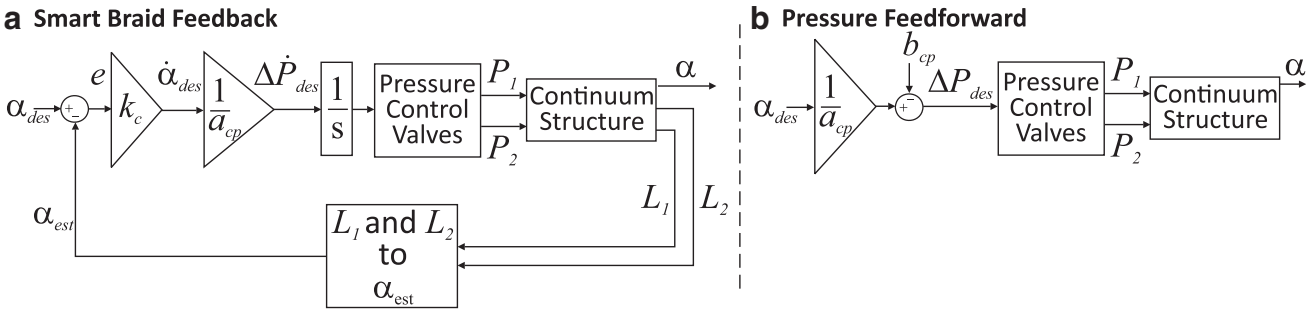

FIG. 14. We compared the performance of two controllers on the continuum manipulator: **(a)** the Smart Braid feedback controller uses tip angle estimates from the inductance-based, Smart Braid sensors and **(b)** a feedforward controller for the actuator pressures.

Feedback control of continuum manipulator

The Smart Braid feedback controller used inductance values and Eq. (23) to estimate the manipulator tip angle α_{est} (Fig. 14a). This estimate was compared against the reference angle α_{des} to calculate the feedback error e

$$e = \alpha_{des} - \alpha_{est}. \tag{26}$$

This error e was scaled by the gain k_c to calculate a desired angular rate $\dot{\alpha}_{des}$

$$\dot{\alpha}_{des} = k_c e. \tag{27}$$

The desired angular rate was again scaled by the inverse of a_{cp} to calculate a desired rate of pressure difference change $\Delta\dot{P}_{des}$ according to the time derivative of Eq. (25)

$$\Delta\dot{P}_{des} = \frac{\dot{\alpha}_{des}}{a_{cp}}. \tag{28}$$

The desired rate of pressure difference change $\Delta\dot{P}_{des}$ was then integrated numerically in the controller to calculate the desired pressure difference ΔP_{des}. The corresponding actuator pressure values were calculated with Eq. (24) and sent to pressure-controlled valves.

For comparison, an open-loop, feedforward controller was implemented that used the inverse of Eq. (25) to generate pressure commands for the actuators (Fig. 14b).

Experimental implementation, continuum manipulator

The continuum manipulator used the same data acquisition and pneumatic control hardware as the revolute joint. The manipulator was fabricated by fastening the outer, conductive braids of the actuators to a flexible spine. The spine consisted of two (0.83 mm thick) strips of Delrin plastic. To establish a ground truth, the angle α of the actuator tip was additionally measured by visually tracking the motion of two points at the actuator tip. The angle of these points was computed relative to two-fixed points on the ground plane. The point positions were recorded with a high-frame-rate camera (120 fps) placed above the manipulator (with the camera's visual field parallel to the plane of actuation). The system pressure was limited to $\sim$0.20 MPa. As with the revolute joint, the Smart Braids were connected in parallel to 390 pF capacitors. For this system, the target inductance sampling rate was 250 Hz.

The value of the gain k_c used in the inductance feedback loop was 5s^{-1}. The performance of controllers was evaluated with the same pseudorandom step input used with the revolute joint. Each controller was evaluated thrice. The steady-state tracking was evaluated over the latter half of each step. That is, the last 5 s of a step lasting 10 s.

Results, continuum manipulator

The inductance feedback controller was able to track the reference signal with a smaller steady-state error than the pressure feedforward controller. Visually tracked tip angle trajectories from typical controller trials are shown in Figure 15. The steady-state RMS error of the inductance feedback controller had an average value of 1.25° and an SD of

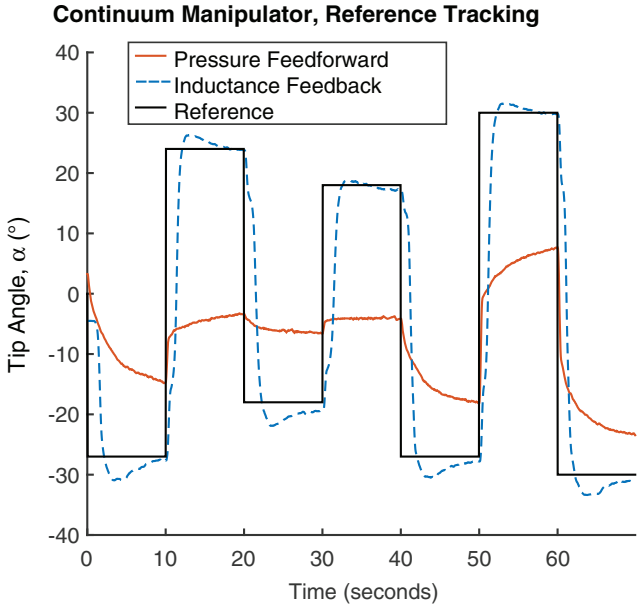

FIG. 15. Shown are the tip angles of the continuum manipulator as recorded by the camera during two trials. The inductance feedback controller allowed the continuum manipulator to track the reference input with an RMS of 1.25° in the steady-state error (evaluated in the last 5 s of the step). Supplementary Video S1 (Supplementary Data are available online at www.liebertpub.com/soro) includes a recording of the inductance feedback trial. Color images available online at www.liebertpub.com/soro

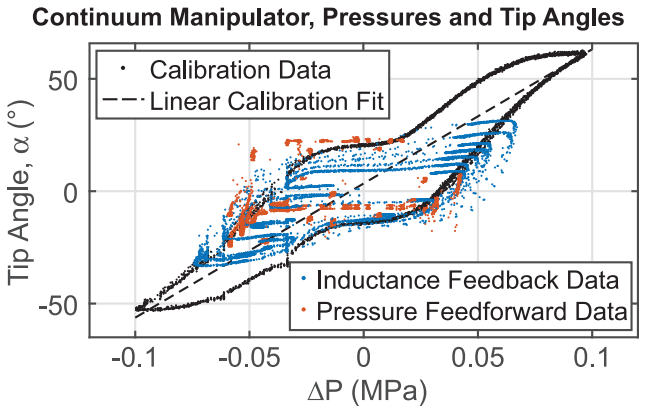

FIG. 16. Shown are tip angles and pressure values observed during the calibration and controlled trials. They exhibited hysteresis and nonlinearity. The *black dots* are the calibration data. The hysteresis is the main obstacle when inverting the calibration curve for open-loop feedforward control. In this article, the inversion was performed on a linear fit to the entire data set (*dashed black line* shown above). The *colored dots* are the data from the angle-control trials. In the controlled trials, the ambiguous relationship between the differential pressure and the tip angle is apparent. Color images available online at www.liebertpub.com/soro

0.63°. On the other hand, the pressure feedforward controller had larger and less consistent steady-state errors (mean of 14.98°, SD of 9.58°). Figure 16 shows the pressure differences and tip angles recorded during the controller trials alongside the calibration data.

Discussion and Conclusions

In this work, we have shown how Smart Braid sensors can be used as feedback for the motion control of soft robotic systems. Smart Braids can provide rapid and precise measurements of actuator length. Motion control was demonstrated in both a revolute system and a bending continuum manipulator. For the revolute joint, we developed techniques to compensate for compliance between actuators and points of motion output. These techniques extend to other actuator length-sensing technologies.

The revolute joint was designed to rigorously compare the Smart Braid feedback to feedback from a rotary encoder. The high-inertia, lightly damped ($I \approx 2\times10^{-3}$ kgm^2, $b \approx 1.2\times10^{-3}$ Nms) rotating load pushed the limits of the controller by creating highly dynamic loads. The results show that, even in this setting, inductance measurements from Smart Braid sensors can be used in real-time feedback control.

When load torques were applied to the revolute joint, the compliance compensation allowed the Smart Braid feedback controller to remain accurate. The addition of an external torque had only a small effect on the performance of the inductance feedback controller. Without the compliance compensation (and given the connection stiffnesses characterized in Table 1), a negative load torque would have led to $\sim3°$ of steady-state error. The less stiff tendon of actuator 2 would have resulted in a 6° error with the positive load torque. With the compliance compensation, the average RMS of the steady-state error in each case was less than 2°.

Controlling the actuators *individually* with the proposed compliance compensation technique sometimes created large tensions in the system. The large preloads could be precluded by controlling the two actuators together with a single controller (as was effectually the case with the encoder feedback).

We also demonstrated Smart Braid feedback on the angle control of a bending continuum manipulator. The feedback used in this work permitted the manipulator to reach desired joint angles using only the inductance measurements from the Smart Braids. The closed-loop control of the manipulator resulted in more accurate reference angle tracking than the simple, open-loop control of pressure. The comparatively poor performance of the open-loop control was due, in part, to hysteresis and unavoidable friction in the system (Fig. 16).

The bend sensing of the continuum manipulator relied on only two sensors. It was limited to approximating the shape of the manipulator as a single segment with constant curvature. This approximation is not necessarily accurate in the presence of external forces and constraints. The constant curvature assumption is most accurate when applied to short segments of the curve.[56] Using Smart Braid sensors on multiple, shorter segments of the actuators could allow more accurate estimation of the end tip position and orientation. Similarly, the principles in this work could be extended to 3D manipulators.

The Smart Braid actuators in this work are slightly different than those used in our previous work. In our prior work, the wires of the Smart Braid sensor served the role of both sensor and reinforcing fiber.[39,40] In our pilot work for this study, we found that the wires bearing the stress of the internal pressure would often yield under high and repeated strain. For this reason, we decided to use Smart Braid sensors on top of a plastic braid that would bear the stress. After 40 h of testing, the sensors showed no signs of wear. The addition of the Smart Braid sensor on top of the inner braid results in disparate length/diameter relationships in the wire braid and the plastic braid. In the revolute joint, this caused the Smart Braid sensor to have a larger diameter than the inner braid in contracted conditions (Fig. 2). In some applications, this would allow relative motion between the two braids, possibly biasing the estimates of the actuator length. A more sophisticated fabrication method could use a single layer of high-strength fibers with long flex life conductors.

Although the fabrication method of the *actuators* was different, the *sensors* were fabricated in the same manner as our previous work.[39] As such, they exhibited a similar sensitivity to the actuator contraction compared to sensors in our previous work. The actuators in our previous work showed contraction sensitivities of 6.8×10^{-8} H/mm[39] and 6.9×10^{-8} H/mm.[40] In this work, the sensitivities of actuators 1 and 2 were 7.4×10^{-8} H/mm and 7.2×10^{-8} H/mm, respectively.

Our results demonstrate that Smart Braids can control the motion of soft robotic systems. The Smart Braid sensors in this work enabled the closed-loop angle control of a revolute joint and a continuum manipulator using local, flexible sensors. It is only through closed-loop control that soft systems can become true autonomous agents, sensing and reacting to their own, changing environment.

Acknowledgments

Funding for this project was provided by NIH (GRANT: 1-R01-EB019834-2014 Wearable eMbots to Induce Recovery of Function). This material is based upon work supported by the National Science Foundation Graduate Research Fellowship under Grant No. DGE 1256260. Any opinion, findings, and conclusions or recommendations expressed in this material are those of the authors(s) and do not necessarily reflect the views of the National Science Foundation.

Author Disclosure Statement

No competing financial interests exist for Khai Yi Chin. Authors C. David Remy and Wyatt Felt are listed as inventors in a relevant patent owned by the University of Michigan (US Patent Application No. 14/743,062). Accordingly, future licenses could lead to revenue distribution according to the policies of the University of Michigan.

References

1. Shepherd RF, Ilievski F, Choi W, Morin SA, Stokes AA, Mazzeo AD, *et al.* Multigait soft robot. Proc Natl Acad Sci U S A 2011;108:400–420.
2. Marchese AD, Onal CD, Rus D. Autonomous soft robotic fish capable of escape maneuvers using fluidic elastomer actuators. Soft Robotics 2014;1:75–87.
3. Polygerinos P, Wang Z, Galloway KC, Wood RJ, Walsh CJ. Soft robotic glove for combined assistance and at-home rehabilitation. Robotics Autonomous Syst 2015;73:135–143.
4. Galloway KC, Becker KP, Phillips B, Kirby J, Licht S, Tchernov D, *et al.* Soft robotic grippers for biological sampling on deep reefs. Soft Robotics 2016;3:23–33.
5. Shapiro Y, Gabor K, Wolf A. Modeling a hyperflexible planar bending actuator as an inextensible euler–bernoulli beam for use in flexible robots. Soft Robotics 2015;2:71–79.
6. Marchese AD, Komorowski K, Onal CD, Rus D. Design and control of a soft and continuously deformable 2D robotic manipulation system. 2014 IEEE International Conference on Robotics and Automation (ICRA), 2014, pp. 2189–2196.
7. Marchese AD, Rus D. Design, kinematics, and control of a soft spatial fluidic elastomer manipulator. Int J Robotics Res 2015;35:840–869.
8. Best CM, Wilson JP, Killpack MD. Control of a pneumatically actuated, fully inflatable, fabric-based, humanoid robot. 2015 IEEE-RAS 15th International Conference on Humanoid Robots (Humanoids), 2015, pp. 1133–1140.
9. Xu R, Asadian A, Naidu AS, Patel RV. Position control of concentric-tube continuum robots using a modified jacobian-based approach. 2013 IEEE International Conference on Robotics and Automation (ICRA), 2013, pp. 5813–5818.
10. Penning RS, Jung J, Ferrier NJ, Zinn MR. An evaluation of closed-loop control options for continuum manipulators. 2012 IEEE International Conference on Robotics and Automation (ICRA), 2012, pp. 5392–5397.
11. Roesthuis RJ, Janssen S, Misra S. On using an array of fiber bragg grating sensors for closed-loop control of flexible minimally invasive surgical instruments. 2013 IEEE/RSJ International Conference on Intelligent Robots and Systems, November 2013, pp. 2545–2551.
12. Trivedi D, Rahn CD, Kier WM, Walker ID. Soft robotics: biological inspiration, state of the art, and future research. Appl Bionics Biomech 2008;5:99–117.
13. Laschi C, Cianchetti M. Soft robotics: new perspectives for robot bodyware and control. Front Bioeng Biotechnol 2014;2:3.
14. Rus D, Tolley MT. Design, fabrication and control of soft robots. Nature 2015;521:467–475.
15. Szelitzky E, Kuklyte J, Mândru D, OConnor N. Low cost angular displacement sensors for biomechanical applications-a review. J Biomed Eng Technol 2014;2:21–28.
16. Sareh S, Noh Y, Li M, Ranzani T, Liu H, Althoefer K. Macrobend optical sensing for pose measurement in soft robot arms. Smart Mater Struct 2015;24:125024.
17. Dobrzynski MK, Pericet-Camara R, Floreano D. Contactless deflection sensor for soft robots. 2011 IEEE/RSJ International Conference on Intelligent Robots and Systems (IROS), 2011, pp. 1913–1918.
18. Ozel S, Keskin NA, Khea D, Onal CD. A precise embedded curvature sensor module for soft-bodied robots. Sens Actuators A Phys 2015;236:349–356.
19. Shapiro Y, Ksa G, Wolf A. Shape tracking of planar hyperflexible beams via embedded pvdf deflection sensors. IEEE/ASME Transactions on Mechatronics 2014;19:1260–1267.
20. Grissom MD, Chitrakaran V, Dienno D, Csencits M, Pritts M, Jones B, *et al.* Design and experimental testing of the octarm soft robot manipulator. Defense and Security Symposium. International Society for Optics and Photonics, 2006, pp. 62301F–362F 301F.
21. Festo. Bionic handling assistant, 2010. Available at: www.festo.com/cms/en_corp/9655_10218.htm (accessed June 2016).
22. Murphy RJ, Otake Y, Taylor RH, Armand M. Predicting kinematic configuration from string length for a snake-like manipulator not exhibiting constant curvature bending. 2014 IEEE/RSJ International Conference on Intelligent Robots and Systems, September 2014, pp. 3515–3521.
23. Rone WS, Ben-Tzvi P. Multi-segment continuum robot shape estimation using passive cable displacement. 2013 IEEE International Symposium on Robotic and Sensors Environments (ROSE), October 2013, pp. 37–42.
24. Askins CG, Miller GA, Friebele EJ. Bend and twist sensing in a multiple-core optical fiber. Optical Fiber Communication Conference/National Fiber Optic Engineers Conference, Optical Society of America, 2008, p. OMT3.
25. Do TN, Tjahjowidodo T, Lau MWS, Phee SJ. Position control of asymmetric nonlinearities for a cable-conduit mechanism. IEEE Trans Autom Sci 2015;PP:1–9.
26. Ledermann C, Mintenbeck J, Ding Y, Pauer H, Wörn H. Closed-loop control of a flexible instrument using an integrated FBG-based shape sensor. International Conference on Advanced Technology & Sciences (ICAT'15), 2015.
27. Ryu SC, Dupont PE. FBG-based shape sensing tubes for continuum robots. 2014 IEEE International Conference on Robotics and Automation (ICRA), 2014, pp. 3531–3537.
28. Culha U, Nurzaman SG, Clemens F, Iida F. Svas3: strain vector aided sensorization of soft structures. Sensors 2014;14:12748–12770.
29. Giffney T, Xie M, Yong A, Wong A, Mousset P, McDaid A, *et al.* Soft pneumatic bending actuator with integrated carbon nanotube displacement sensor. Robotics 2016;5:7.
30. Park Y-L, Wood RJ. Smart pneumatic artificial muscle actuator with embedded microfluidic sensing. 2013 IEEE on Sensors, 2013, pp. 1–4.

31. Chossat JB, Park YL, Wood RJ, Duchaine V. A soft strain sensor based on ionic and metal liquids. IEEE Sens J 2013;13:3405–3414.
32. Russo S, Ranzani T, Liu H, Nefti-Meziani S, Althoefer K, Menciassi A. Soft and stretchable sensor using biocompatible electrodes and liquid for medical applications. Soft Robotics 2015;2:146–154.
33. Cianchetti M, Renda F, Licofonte A, Laschi C. Sensorization of continuum soft robots for reconstructing their spatial configuration. In: Biomedical Robotics and Biomechatronics (BioRob), 2012 4th IEEE RAS & EMBS International Conference, 2012, pp. 634–639.
34. Veale AJ, Anderson IA, Xie SQ. The smart peano fluidic muscle: a low profile flexible orthosis actuator that feels pain. In: SPIE Smart Structures and Materials+ Nondestructive Evaluation and Health Monitoring. International Society for Optics and Photonics 2015, pp. 94 351V–394V 351 V.
35. Nakamoto H, Oida S, Ootaka H, Tada M, Hirata I, Kobayashi F, *et al*. Application of stretchable strain sensor for pneumatic artificial muscle. Robotic Intelligence in Informationally Structured Space (RiiSS), 2014 IEEE Symposium, 2014, pp. 1–5.
36. Stretch Sense. Available at: www.stretchsense.com (accessed April 2016).
37. Zhang H, Wang MY. Multi-axis soft sensors based on dielectric elastomer. Soft Robotics 2016;3:3–12.
38. Anderson IA, Gisby TA, McKay TG, OBrien BM, Calius EP. Multi-functional dielectric elastomer artificial muscles for soft and smart machines. J Appl Phys 2012;112.
39. Felt W, Chin KY, Remy CD. Contraction sensing with smart braid mckibben muscles. IEEE/ASME Transactions on Mechatronics 2016;21:1201–1209.
40. Felt W, Remy CD. Smart braid: air muscles that measure force and displacement. 2014 IEEE/RSJ International Conference on Intelligent Robots and Systems (IROS 2014), 2014, pp. 2821–2826.
41. Felt W, Suen M, Remy CD. Sensing the motion of bellows through changes in mutual inductance. 2016 IEEE/RSJ International Conference on Intelligent Robots and Systems (IROS 2016), 2016.
42. Schulte H. The characteristics of the mckibben artificial muscle. The application of external power in prosthetics and orthotics. 1961;874:94–115.
43. Chou C-P, Hannaford B. Measurement and modeling of mckibben pneumatic artificial muscles. IEEE Transactions on Robotics and Automation 1996;12:90–102.
44. Ueda J, Ming D, Krishnamoorthy V. Individual muscle control using an exoskeleton robot for muscle function testing. IEEE Transactions on Neural Systems and Rehabilitation Engineering 2010;18:339–350.
45. Wehner M, Quinlivan B, Aubin PM, Martinez-Villalpando E, Baumann M, Stirling L, *et al.* A lightweight soft exosuit for gait assistance. 2013 IEEE International Conference on Robotics and Automation (ICRA), 2013, pp. 3362–3369.
46. Ando T, Kobayashi Y, Okamoto J, Takahashi M, Fujie MG. Intelligent trunk corset to support rollover of cancer bone metastasis patients. IEEE/ASME Transactions on Mechatronics, 2010;15:181–190.
47. Sun Z, Bao G, Yang Q, Wang Z. Design of a novel force feedback dataglove based on pneumatic artificial muscles. Proceedings of the 2006 IEEE International Conference on Mechatronics and Automation, 2006, pp. 968–972.
48. Andrikopoulos G, Nikolakopoulos G, Manesis S. A survey on applications of pneumatic artificial muscles. 2011 19th Mediterranean Conference on Control Automation (MED), June 2011, pp. 1439–1446.
49. Pritts MB, Rahn CD. Design of an artificial muscle continuum robot. 2004 IEEE International Conference on Robotics and Automation 2004;5:4742–4746.
50. Bartow A, Kapadia A, Walker I. A novel continuum trunk robot based on contractor muscles. Proceedings of the 12th WSEAS International Conference on Signal Processing, Robotics, and Automation, 2013, pp. 181–186.
51. Felt W, Chin KY, Remy CD. Dynamic tracking of joint motion with antagonized smart braids. Fluid Power Innovation & Research Conference (FPIRC 2015), 2015.
52. Tondu B, Lopez P. Modeling and control of mckibben artificial muscle robot actuators. IEEE Control Systems 2000; 20:15–38.
53. Texas Instruments. LDC1000 Inductance-to-Digital Converter, Compare, 2015. Available at: www.ti.com/product/LDC1000/compare (accessed June 2016).
54. Lambeck S, Busch C. Exact linearization control for a pneumatic proportional pressure control valve. 2010 8th IEEE International Conference on Control and Automation (ICCA), 2010, pp. 22–27.
55. McCormack A, Godfrey K. Rule-based autotuning based on frequency domain identification. IEEE Transactions on Control Systems Technology 1998;6:43–61.
56. Webster RJ, Jones BA. Design and kinematic modeling of constant curvature continuum robots: a review. Int J Robotics Res 2010;29:1661–1683.

Address correspondence to:
Wyatt Felt
Robotics and Motion Laboratory (RAMlab)
Department of Mechanical Engineering
University of Michigan
Ann Arbor, MI 48109

E-mail: wfelt@umich.edu